

An Efficient Multigrid Solver based on Distributive Smoothing for Poroelasticity Equations

R. Wienands, Köln, **F.J. Gaspar**, Zaragoza,
F.J. Lisbona, Zaragoza, and **C.W. Oosterlee**, Delft

Received February 20, 2004; revised April 13, 2004
Published online: June 21, 2004 2004
© Springer-Verlag 2004

Abstract

In this paper, we present a robust distributive smoother in a multigrid method for the system of poroelasticity equations. Within the distributive framework, we deal with a decoupled system, that can be smoothed with basic iterative methods like an equation-wise red-black Jacobi point relaxation. The properties of the distributive relaxation are optimized with the help of Fourier smoothing analysis. A highly efficient multigrid method results, as is confirmed by Fourier two-grid analysis and numerical experiments.

AMS Subject Classification: 65N55, 74F10, 74S10, 65M12.

Keywords: Poroelasticity, staggered discretization, multigrid, distributive relaxation, local Fourier analysis.

1. Introduction

Poroelasticity theory addresses the time dependent coupling between the deformation of porous material and the fluid flow inside. The porous matrix is supposed to be saturated by the fluid phase. The state of this continuous medium is characterized by the knowledge of elastic displacements and fluid pressure at each point. A phenomenological model for a rather general situation was first proposed and analyzed by Biot [1], studying the consolidation of soils. Poroelastic models are used nowadays to study problems in geomechanics, hydrogeology, petrol engineering and biomechanics [9,4].

In this paper, we present an efficient multigrid method for the system of poroelasticity equations. In particular, we introduce a robust point-wise smoothing method based on distributive iteration. In distributive smoothing the original system of equations is transformed by post-conditioning in order to achieve favorable properties, such as a decoupling of the equations and/or possibilities for point-wise smoothing. A specialty lies in the discretization approach employed. We adopt a staggered grid for the poroelasticity equations as in [5,6]. A popular alternative is to use finite elements, see, for example, [10] for the quasi-static

problem, or [12] for the dynamic problem. Standard finite differences do not lead to stable solutions without additional stabilization. Throughout this paper we concentrate on Cartesian equidistant grids.

The multigrid method is developed on the basis of Fourier analysis of increasing complexity [2], [14]. The h -ellipticity concept is discussed, which is fundamental for the existence of point-wise smoothers. The distributive smoother is developed based on insights from the Stokes and incompressible Navier-Stokes equations [2], [3], [14], [18]. Optimal relaxation parameters are obtained with smoothing analysis, leading to a relaxation method, that is robust w.r.t. the problem parameters like Lamé coefficients, permeability of the porous medium, viscosity of the fluid, and time step and grid size. Furthermore, the multigrid method is analyzed by Fourier two-grid analysis [2], [13], [14] demonstrating an efficient interplay between relaxation and coarse grid correction.

The outline of this paper is as follows. The model and discretization are described in Sect. 2. In Sect. 3, the separate components of the multigrid solution method are presented and analyzed in different subsections; in Sect. 3.2 the h -ellipticity measure of the discretization, in Sects. 3.3 and 3.4 the relaxation method, and in Sect. 3.5 the coarse grid correction. Numerical multigrid results are presented in Sect. 4, confirming the theoretical considerations.

2. Mathematical Model and Discretization

2.1. Continuous System

The poroelastic model can be formulated as a system of partial differential equations for displacements and the pressure of the fluid. One assumes the material's solid structure to be linearly elastic, initially homogeneous and isotropic, the strains imposed within the material are small. We denote by $\mathbf{u} = (u, v, p)^T$ the solution vector, consisting of the displacement vector $\bar{\mathbf{u}} = (u, v)^T$ and pore pressure of the fluid p . The incompressible, two-dimensional variant of Biot's consolidation model reads

$$\begin{aligned} -(\lambda + 2\mu)u_{xx} - \mu u_{yy} - (\lambda + \mu)v_{xy} + p_x &= 0, \\ -(\lambda + \mu)u_{xy} - \mu v_{xx} - (\lambda + 2\mu)v_{yy} + p_y &= 0, \\ (u_x + v_y)_t - a(p_{xx} + p_{yy}) &= Q \end{aligned} \tag{1}$$

(plus initial and boundary conditions) with $\lambda, \mu (\geq 0)$ the Lamé coefficients, $a = \kappa/\eta \geq 0$ with κ the permeability of the porous medium and η the viscosity of the fluid, and Q the source (representing an injection or extraction process), see [1]. Problem (1) is a limit of the compressible case. The compressible system will be easier to solve, however, due to an extra contribution to the main diagonal of the matrix related to this system. We concentrate on a solver for the two-dimensional incompressible case, and focus on a *model operator* \mathbf{L} which is suitable for analysis. It reads

$$\mathbf{L} = \begin{pmatrix} -(\lambda + 2\mu)\partial_{xx} - \mu\partial_{yy} & -(\lambda + \mu)\partial_{xy} & \partial_x \\ -(\lambda + \mu)\partial_{xy} & -\mu\partial_{xx} - (\lambda + 2\mu)\partial_{yy} & \partial_y \\ \partial_x & \partial_y & -\tilde{a}(\partial_{xx} + \partial_{yy}) \end{pmatrix}. \quad (2)$$

\mathbf{L} can be interpreted as a “stationary variant” of (1), i.e., the operator after an implicit (semi-) discretization in time. For example, in case of Crank-Nicholson time discretization we have $\tilde{a} = 0.5a\delta t$. From (2), one may calculate the corresponding determinant:

$$\det(\mathbf{L}) = -\mu\Delta(\tilde{a}(\lambda + 2\mu)\Delta^2 - \Delta)$$

with Laplace operator Δ and biharmonic operator Δ^2 . The principal part of $\det(\mathbf{L})$ is Δ^m with m depending on the choice of λ , μ , and \tilde{a} . Due to physical reasons, we always have $\mu, \tilde{a}, \lambda + 2\mu > 0$, yielding $m = 3$. The number of boundary conditions that must accompany \mathbf{L} is m [2,14].

A dimensionless version of (1) can be obtained with dimensionless parameters:

$$\hat{\mu} = 1 + (\lambda/\mu) \quad (= 1/(1 - 2\nu), \quad \text{with Poisson ratio } \nu), \quad (3)$$

$\hat{x} = x/\ell$, $\hat{y} = y/\ell$, $\hat{t} = (\lambda + 2\mu)at/\ell^2$, $\hat{Q} = \ell^2 Q/(a(\lambda + 2\mu))$, and unknowns $\hat{u} = u/\ell$, $\hat{v} = v/\ell$, $\hat{p} = p/(\lambda + 2\mu)$. Here, scaling has taken place with respect to a characteristic length of the porous medium ℓ , the Lamé constant $\lambda + 2\mu$, time scale t_0 , and a in (1).

2.2. Discrete System

The time-dependent operator (2) suffers from stability difficulties. The coefficient in the $L^{3,3}$ -block in (2) is typically, depending on the time step, extremely small. In order to avoid oscillating solutions, the discretization has to be designed with care. To overcome the stability difficulties in finite differences, a staggered grid was proposed in [5], [6]. We adopt this methodology for system (1), using central differences on a uniform staggered grid with mesh size h . Staggering is, of course, a well-known discretization technique in computational fluid dynamics, in particular for incompressible flow [8], [16].

Often in poroelasticity problems pressure values are prescribed at the physical boundary. So, pressure points in the staggered grid should be located at the physical boundary, and the displacement points are then defined at the cell faces. Therefore, a divergence operator is naturally approximated by a central discretization of the displacements in a cell, see Fig. 1. Notice that the staggered placement of unknowns here is different from incompressible Navier-Stokes, because of the pressure placement. The two-dimensional (infinite) staggered grid employed is composed of three types of grid points, $G_h = G_h^1 \cup G_h^2 \cup G_h^3$, where

$$G_h^j := \{\mathbf{x}_h^j = (x_h^j, y_h^j) := (k_x, k_y)h + s^j; (k_x, k_y) \in \mathbb{Z}^2\}, \quad (4)$$

with

$$u - \text{grid points } \mathbf{x}_h^1 \in G_h^1 \text{ with } s^1 = (h/2, 0),$$

$$v - \text{grid points } \mathbf{x}_h^2 \in G_h^2 \text{ with } s^2 = (0, h/2),$$

$$p - \text{grid points } \mathbf{x}_h^3 \in G_h^3 \text{ with } s^3 = (0, 0)$$

and a uniform mesh size h , see Fig. 1.

The discrete system

$$\mathbf{L}_h \mathbf{u}_h = \begin{pmatrix} L_h^{1,1} & L_h^{1,2} & L_h^{1,3} \\ L_h^{2,1} & L_h^{2,2} & L_h^{2,3} \\ L_h^{3,1} & L_h^{3,2} & L_h^{3,3} \end{pmatrix} \begin{pmatrix} u_h(\mathbf{x}_h^1) \\ v_h(\mathbf{x}_h^2) \\ p_h(\mathbf{x}_h^3) \end{pmatrix} = \mathbf{f}_h. \quad (5)$$

based on (2) reads at u -grid points:

$$-(\lambda + 2\mu)(\partial_{xx})_h u_h - \mu(\partial_{yy})_h u_h - (\lambda + \mu)(\partial_{xy})_{h/2} v_h + (\partial_x)_{h/2} p_h = 0, \quad (6)$$

at v -grid points:

$$-(\lambda + \mu)(\partial_{xy})_{h/2} u_h - \mu(\partial_{xx})_h v_h - (\lambda + 2\mu)(\partial_{yy})_h v_h + (\partial_y)_{h/2} p_h = 0, \quad (7)$$

and at p -grid points:

$$(\partial_x)_{h/2} u_h + (\partial_y)_{h/2} v_h - \tilde{a}(\partial_{xx})_h p_h - \tilde{a}(\partial_{yy})_h p_h = Q. \quad (8)$$

Here, the following discrete operators on the staggered grid (4) are used (given in stencil notation):

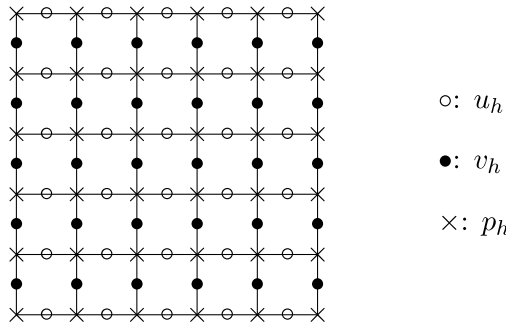


Fig. 1. Staggered location of unknowns for poroelasticity

$$\begin{aligned}
 (\partial_x)_{h/2} &\triangleq \frac{1}{h} [-1 \quad \star \quad 1]_{h/2}, & -(\partial_{xx})_h &\triangleq \frac{1}{h^2} [-1 \quad 2 \quad -1]_h, \\
 (\partial_{xy})_{h/2} &\triangleq \frac{1}{h^2} \begin{bmatrix} -1 & & 1 \\ & \star & \\ 1 & & -1 \end{bmatrix}_{h/2}.
 \end{aligned}$$

The “ \star ” denotes the position on the shifted grids G_h^1 and G_h^2 at which the stencil is applied, compare with Fig. 1. $(\partial_y)_{h/2}$ and $-(\partial_{yy})_h$ are given by analogous stencils.

We choose the Crank-Nicolson discretization in time direction, with $O(\delta t^2)$ accuracy. Second-order accuracy has been obtained for reference problems with smooth solutions (not shown here).

3. Multigrid Solution Method

In this context, an efficient solver for the system of poroelasticity equations discretized on staggered grids is necessary. Multigrid methods (see, for example, [2,7,14]) are motivated by two basic observations: Firstly many iterative methods have a strong error smoothing effect if they are applied to discrete elliptic problems $L_h \mathbf{u}_h = \mathbf{f}_h$. Secondly, a smooth error term can be well represented on a coarser grid where its approximation is substantially less expensive. These observations suggest the following structure of a two-grid cycle for a linear problem, called the correction scheme: Perform n_1 steps of an iterative relaxation method S_h on the fine grid (pre-smoothing), compute the defect of the current fine grid approximation, restrict the defect to the coarse grid using a restriction operator $R_{h,2h}$, solve the coarse grid defect equation, interpolate the correction using a prolongation operator $P_{2h,h}$ to the fine grid, add the interpolated correction to the current fine grid approximation (coarse grid correction), perform n_2 steps of an iterative relaxation method on the fine grid (post-smoothing). Hence, the two-grid error transformation operator is given by

$$M_{h,2h} := S_h^{n_2} \left(I_h - P_{2h,h} (L_{2h})^{-1} R_{h,2h} L_h \right) S_h^{n_1} = S_h^{n_2} C_{h,2h} S_h^{n_1}, \quad (9)$$

where I_h denotes the identity and $C_{h,2h}$ is called the coarse grid correction operator. Instead of inverting L_{2h} , the coarse grid equation can be solved by a recursive application of this procedure, yielding a multigrid method. We assume standard coarsening here, i.e., the sequence of coarse grids is obtained by repeatedly doubling the mesh size in each space direction. This is indicated by the subscript “ $2h$ ”.

The crucial point for any multigrid method is to identify the multigrid components yielding an efficient interplay between relaxation and coarse grid correction. A useful tool for a proper selection is local Fourier analysis.

3.1. Basic Elements of Local Fourier Analysis for Multigrid

Classical Fourier analysis [2], [13], [14] is often applied to develop efficient multigrid methods for linear elliptic equations with constant (or frozen) coefficients. It is based on the simplification that boundary conditions are neglected and all occurring operators are extended to an infinite grid. On an infinite grid, the discrete solution, its current approximation and the corresponding error or residual can be represented by linear combinations of certain exponential functions - the Fourier components - which form a unitary basis of the space of bounded infinite grid functions. On the staggered grid G_h under consideration, a unitary basis of vector-valued Fourier components is given by

$$\boldsymbol{\varphi}_h(\boldsymbol{\theta}, \bar{\mathbf{x}}_h) := \begin{pmatrix} \exp(i\boldsymbol{\theta} \cdot \mathbf{x}_h^1/h) \\ \exp(i\boldsymbol{\theta} \cdot \mathbf{x}_h^2/h) \\ \exp(i\boldsymbol{\theta} \cdot \mathbf{x}_h^3/h) \end{pmatrix} \text{ with } \boldsymbol{\theta} \in \Theta := (-\pi, \pi]^2, \\ \bar{\mathbf{x}}_h := (\mathbf{x}_h^1, \mathbf{x}_h^2, \mathbf{x}_h^3), \quad \mathbf{x}_h^j \in G_h^j, (j = 1, 2, 3)$$

and complex unit $i = \sqrt{-1}$ yielding the Fourier space

$$F(G_h) := \text{span}\{\boldsymbol{\varphi}_h(\boldsymbol{\theta}, \bar{\mathbf{x}}_h) : \boldsymbol{\theta} \in \Theta\}.$$

(For scalar equations defined, for example, on G_h^3 , the corresponding Fourier components read $\varphi_h(\boldsymbol{\theta}, \mathbf{x}_h^3) := \exp(i\boldsymbol{\theta} \cdot \mathbf{x}_h^3/h)$.) Then, the main idea of local Fourier analysis is to analyze different multigrid components by evaluating their effect on the Fourier components.

If standard coarsening in two dimensions is selected, each ‘‘low-frequency’’

$$\boldsymbol{\theta} = \boldsymbol{\theta}^{00} \in \Theta_{\text{low}}^{2h} := (-\pi/2, \pi/2]^2$$

is coupled with three ‘‘high-frequencies’’

$$\boldsymbol{\theta}^{11} := \boldsymbol{\theta}^{00} - (\text{sign}(\theta_1), \text{sign}(\theta_2))\pi, \quad \boldsymbol{\theta}^{10} := \boldsymbol{\theta}^{00} - (\text{sign}(\theta_1), 0)\pi, \\ \boldsymbol{\theta}^{01} := \boldsymbol{\theta}^{00} - (0, \text{sign}(\theta_2))\pi \quad \left(\boldsymbol{\theta}^{11}, \boldsymbol{\theta}^{10}, \boldsymbol{\theta}^{01} \in \Theta_{\text{high}}^{2h} := \Theta \setminus \Theta_{\text{low}}^{2h} \right)$$

in the transition from G_h to G_{2h} . That is, the related three high-frequency components are not visible on the coarse grid G_{2h} as they coincide with the coupled low-frequency component. Now, the Fourier space can be subdivided into the corresponding four-dimensional subspaces, known as $2h$ -harmonics:

$$F_{2h}(\boldsymbol{\theta}) := \text{span}\{\boldsymbol{\varphi}_h(\boldsymbol{\theta}^{00}, \bar{\mathbf{x}}_h), \boldsymbol{\varphi}_h(\boldsymbol{\theta}^{11}, \bar{\mathbf{x}}_h), \boldsymbol{\varphi}_h(\boldsymbol{\theta}^{10}, \bar{\mathbf{x}}_h), \boldsymbol{\varphi}_h(\boldsymbol{\theta}^{01}, \bar{\mathbf{x}}_h)\} \quad (10)$$

with $\boldsymbol{\theta} = \boldsymbol{\theta}^{00} \in \Theta_{\text{low}}^{2h}$.

3.2. Measure of h -Ellipticity for the Fine Grid Discretization \mathbf{L}_h

The h -ellipticity measure is often used to decide whether or not a certain discretization is appropriate for a multigrid treatment. A “sufficient” amount of h -ellipticity (some form of “ellipticity” in the discretization) indicates that pointwise error smoothing procedures can be constructed [2], [3], [14]. The measure of h -ellipticity for the (3×3) -system of equations is defined by

$$E_h(\mathbf{L}_h) := \frac{\min \left\{ |\det(\tilde{\mathbf{L}}_h(\boldsymbol{\theta}))| : \boldsymbol{\theta} \in \Theta_{\text{high}}^{2h} \right\}}{\max \left\{ |\det(\tilde{\mathbf{L}}_h(\boldsymbol{\theta}))| : \boldsymbol{\theta} \in \Theta \right\}},$$

where the complex (3×3) -matrix $\tilde{\mathbf{L}}_h(\boldsymbol{\theta})$ is the Fourier symbol of \mathbf{L}_h , i.e.,

$$\mathbf{L}_h \boldsymbol{\varphi}_h(\boldsymbol{\theta}, \bar{\mathbf{x}}_h) = \tilde{\mathbf{L}}_h(\boldsymbol{\theta}) \boldsymbol{\varphi}_h(\boldsymbol{\theta}, \bar{\mathbf{x}}_h).$$

The determinant of the discrete version of (2) is given by

$$\det(\mathbf{L}_h) = -\mu \Delta_h (\tilde{a}(\lambda + 2\mu) \Delta_h^2 - \Delta_h),$$

where the discrete Laplacian and the discrete biharmonic operator are represented by the following stencils

$$-\Delta_h \stackrel{\wedge}{=} \frac{1}{h^2} \begin{bmatrix} & & & & \\ & -1 & & & \\ -1 & 4 & -1 & & \\ & & -1 & & \\ & & & & \end{bmatrix}_h, \quad \Delta_h^2 \stackrel{\wedge}{=} \frac{1}{h^4} \begin{bmatrix} & & & & & & \\ & & & & & & \\ & & & 1 & & & \\ & & 2 & -8 & 2 & & \\ 1 & -8 & 20 & -8 & 1 & & \\ & & 2 & -8 & 2 & & \\ & & & & & & \\ & & & & & & 1 \\ & & & & & & \end{bmatrix}_h. \quad (11)$$

Theorem 1. *The measure of h -ellipticity for the discrete system of poroelasticity equations ((6), (7), (8)) is given by*

$$E_h(\mathbf{L}_h) = \frac{2\tilde{a}(\lambda + 2\mu) + h^2}{128\tilde{a}(\lambda + 2\mu) + 16h^2}.$$

Proof: The Fourier symbols of the discrete *scalar* operators (which are analogously defined as for systems above, see [2], [14] for details) read,

$$\left(\tilde{\partial}_x \right)_{h/2}(\boldsymbol{\theta}) = 1s_1, \quad -\left(\tilde{\partial}_{xx} \right)_h(\boldsymbol{\theta}) = s_1^2, \quad -\tilde{\Delta}_h(\boldsymbol{\theta}) = s_1^2 + s_2^2 \quad (12)$$

$$\left(\tilde{\partial}_{xy} \right)_{h/2}(\boldsymbol{\theta}) = -s_1s_2, \quad \tilde{\Delta}_h^2(\boldsymbol{\theta}) = (s_1^2 + s_2^2)^2, \quad (13)$$

where $s_1 := \frac{2}{h} \sin(\theta_1/2)$ and $s_2 := \frac{2}{h} \sin(\theta_2/2)$. (The operators in the y -direction go similarly.) The Fourier symbol of the system and its determinant read

$$\tilde{\mathbf{L}}_h(\boldsymbol{\theta}) = \begin{pmatrix} (\lambda + 2\mu)s_1^2 + \mu s_2^2 & -(\lambda + \mu)s_1 s_2 & i s_1 \\ -(\lambda + \mu)s_1 s_2 & \mu s_1^2 + (\lambda + 2\mu)s_2^2 & i s_2 \\ i s_1 & i s_2 & \tilde{a}(s_1^2 + s_2^2) \end{pmatrix},$$

$$\det(\tilde{\mathbf{L}}_h(\boldsymbol{\theta})) = \mu(s_1^2 + s_2^2) \left(\tilde{a}(\lambda + 2\mu)(s_1^2 + s_2^2)^2 + s_1^2 + s_2^2 \right). \quad (14)$$

Due to $\lambda, \mu, \tilde{a} \geq 0$ and the definition of s_1 and s_2 it follows from (14) that $\max_{\boldsymbol{\theta} \in \Theta} \left\{ \det(\tilde{\mathbf{L}}_h(\boldsymbol{\theta})) \right\}$ is obtained at $\boldsymbol{\theta}_{\max} = (\pi, \pi)$ leading to

$$\det(\tilde{\mathbf{L}}_h(\boldsymbol{\theta}_{\max})) = \frac{64}{h^6} \mu (8\tilde{a}(\lambda + 2\mu) + h^2). \quad (15)$$

Similarly, $\min_{\boldsymbol{\theta} \in \Theta_{\text{high}}} \left\{ \det(\tilde{\mathbf{L}}_h(\boldsymbol{\theta})) \right\}$ is obtained at $\boldsymbol{\theta}_{\min} = (\pi/2, 0), (0, \pi/2)$ yielding

$$\det(\tilde{\mathbf{L}}_h(\boldsymbol{\theta}_{\min})) = \frac{4}{h^6} \mu (2\tilde{a}(\lambda + 2\mu) + h^2). \quad (16)$$

Combining (15) and (16) concludes the proof. \square

Thus, $E_h(\mathbf{L}_h)$ is uniformly bounded away from zero for all reasonable combinations of $\lambda, \mu, \tilde{a} \geq 0$ and $h > 0$. As a consequence, it should be possible to find efficient *point-wise* smoothers within a multigrid method. This may be surprising, because $L_h^{1,1}$ and $L_h^{2,2}$ from (5) may contain *grid anisotropies* depending on the choice of the Lamé coefficients. That is, the size of the coefficients referring to the different spatial directions (i.e., $-(\lambda + 2\mu)$ and $-\mu$) may vary considerably. Apparently, the smoothing properties of a proper point relaxation scheme for the system are not affected by these scalar grid anisotropies. For a vanishing mesh size one obtains

$$\lim_{h \rightarrow 0} E_h(\mathbf{L}_h) = \frac{1}{64} > 0$$

implying that the above considerations are valid in the limit of small mesh size as well.

3.3. Distributive Relaxation S_h

We construct a distributive relaxation for the discrete system \mathbf{L}_h . In order to relax $\mathbf{L}_h \mathbf{u}_h = \mathbf{f}_h$, we introduce a new variable \mathbf{w}_h by $\mathbf{u}_h = \mathbf{C}_h \mathbf{w}_h$ and consider the transformed system $\mathbf{L}_h \mathbf{C}_h \mathbf{w}_h = \mathbf{f}_h$. Ideally (compare with [2]), \mathbf{C}_h is chosen such that the resulting system $\mathbf{L}_h \mathbf{C}_h$ is triangular and the diagonal elements of $\mathbf{L}_h \mathbf{C}_h$ are composed of $\det(\mathbf{L}_h)$. Then, the resulting transformed system is suited for *decoupled* smoothing, i.e., each equation can be treated separately. The new contribution here is the following choice for the distributor

$$\mathbf{C}_h = \begin{pmatrix} I_h & 0 & -(\partial_x)_{h/2} \\ 0 & I_h & -(\partial_y)_{h/2} \\ (\lambda + \mu)(\partial_x)_{h/2} & (\lambda + \mu)(\partial_y)_{h/2} & -(\lambda + 2\mu)\Delta_h \end{pmatrix} \quad (17)$$

with identity I_h . Then, the transformed system for the interior points (Remarks 1 and 2 refer to the boundaries) reads

$$\mathbf{L}_h \mathbf{C}_h = \begin{pmatrix} -\mu\Delta_h & 0 & 0 \\ 0 & -\mu\Delta_h & 0 \\ LC_h^{3,1} & LC_h^{3,2} & \tilde{a}(\lambda + 2\mu)\Delta_h^2 - \Delta_h \end{pmatrix} \quad \text{with} \quad (18)$$

$$LC_h^{3,1} = (\partial_x)_{h/2} - \tilde{a}(\lambda + \mu) \left((\partial_{xxx})_{h/2} + (\partial_{xyy})_{h/2} \right) \quad \text{and} \quad (19)$$

$$LC_h^{3,2} = (\partial_y)_{h/2} - \tilde{a}(\lambda + \mu) \left((\partial_{xxy})_{h/2} + (\partial_{yyx})_{h/2} \right), \quad (20)$$

where the central discrete operators read in stencil notation

$$(\partial_x)_{h/2} \stackrel{\wedge}{=} \frac{1}{h} \begin{bmatrix} -1 & \star & 1 \end{bmatrix}_{h/2}, \quad (\partial_{xxx})_{h/2} \stackrel{\wedge}{=} \frac{1}{h^3} \begin{bmatrix} -1 & 3 & \star & -3 & 1 \end{bmatrix}_{h/2},$$

$$(\partial_{xxy})_{h/2} \stackrel{\wedge}{=} \frac{1}{h^3} \begin{bmatrix} 1 & -2 & 1 \\ & \star & \\ -1 & 2 & -1 \end{bmatrix}_{h/2}.$$

The other discrete operators are given by analogous stencils.

For an implementation of the distributive relaxation it is convenient to consider the *correction* equations

$$\mathbf{L}_h \delta \mathbf{u}^{m+1} = \mathbf{r}_h^m \quad \text{and} \quad \mathbf{L}_h \mathbf{C}_h \delta \mathbf{w}^{m+1} = \mathbf{r}_h^m$$

with update $\delta \mathbf{u}^{m+1} = \mathbf{C}_h \delta \mathbf{w}^{m+1} = \mathbf{u}_h - \mathbf{u}_h^{m+1}$ and residual $\mathbf{r}_h^m = \mathbf{L}_h \mathbf{u}_h^m - \mathbf{f}_h$. \mathbf{u}_h^m denotes the approximation after the m th iteration of the exact discrete solution \mathbf{u}_h .

The distributive relaxation consists of two steps. In the first step, a new approximation $\delta \mathbf{w}^{m+1}$ to the ‘‘ghost variable’’ $\delta \mathbf{w} = (\delta w_u, \delta w_v, \delta w_p)^T$ is calculated. This will be done by decoupled red-black point relaxation, due to the structure of the transformed system $\mathbf{L}_h \mathbf{C}_h$; discussed in Sect. 4. In the second step, a new approximation for \mathbf{u}_h is computed by

$$\mathbf{u}_h^{m+1} = \mathbf{u}_h^m + \delta \mathbf{u}_h^{m+1} = \mathbf{u}_h^m + \mathbf{C}_h \delta \mathbf{w}^{m+1}. \quad (21)$$

In detail, the new approximation in (21) is given by

$$\begin{aligned} u_h^{m+1} &= u_h^m + \delta w_u^{m+1} - (\partial_x)_{h/2} \delta w_p^{m+1}, \\ v_h^{m+1} &= v_h^m + \delta w_v^{m+1} - (\partial_y)_{h/2} \delta w_p^{m+1}, \\ p_h^{m+1} &= p_h^m + (\lambda + \mu)(\partial_x)_{h/2} \delta w_u^{m+1} + (\lambda + \mu)(\partial_y)_{h/2} \delta w_v^{m+1} \\ &\quad - (\lambda + 2\mu)\Delta_h \delta w_p^{m+1}. \end{aligned}$$

This implementation is straightforward.

Remark 1. The distributive relaxation operations described above ((17), (18)) are operator manipulations in which the discretization of boundary operators is not taken into account explicitly. Experience with distributive relaxation gained in computational fluid dynamics learns that the zero blocks in (18) may not always equal zero exactly for certain boundary conditions. Therefore, it is often advised to perform additional relaxation steps near boundaries. In the application presented here, we do not need the additional treatment near the boundary.

Remark 2. A “left distributor” for $C_h L_h \mathbf{u}_h = C_h \mathbf{f}_h$ may read:

$$C_h = \begin{pmatrix} I_h & 0 & (\lambda + \mu)(\partial_x)_{h/2} \\ 0 & I_h & (\lambda + \mu)(\partial_y)_{h/2} \\ -(\partial_x)_{h/2} & -(\partial_y)_{h/2} & -(\lambda + 2\mu)\Delta_h \end{pmatrix}.$$

In that case, we obtain

$$C_h L_h = \begin{pmatrix} -\mu\Delta_h & 0 & LC_h^{1,3} \\ 0 & -\mu\Delta_h & LC_h^{2,3} \\ 0 & 0 & \tilde{a}(\lambda + 2\mu)\Delta_h^2 - \Delta_h \end{pmatrix}$$

with $LC_h^{1,3} = LC_h^{3,1}$ and $LC_h^{2,3} = LC_h^{3,2}$; see (19), (20). We end up with an upper triangular system. In a first step then, the last equation should be updated after which the other two may be treated. The advantage of a left distributor may be that we still deal with the primary unknowns \mathbf{u}_h , whereas in the right distributor case we work with \mathbf{w}_h as the slack variable. A disadvantage of a left distributor is that the right-hand side must also be transformed. We have chosen for the right distributor as we do not encounter any problems in defining boundary conditions here. Also in the case of stress boundary conditions, treated in a future paper, it is easily possible to set up the distributive system near the boundaries.

Remark 3. For the discrete Stokes operator

$$L_{h,st} = \begin{pmatrix} -\Delta_h & 0 & (\partial_x)_{h/2} \\ 0 & -\Delta_h & (\partial_y)_{h/2} \\ (\partial_x)_{h/2} & (\partial_y)_{h/2} & 0 \end{pmatrix}$$

the distributor proposed in [3], [18] is given by

$$\mathbf{C}_{h,st} = \begin{pmatrix} I_h & 0 & -(\partial_x)_{h/2} \\ 0 & I_h & -(\partial_y)_{h/2} \\ 0 & 0 & -\Delta_h \end{pmatrix}.$$

The transformed system then reads

$$\mathbf{L}_{h,st} \mathbf{C}_{h,st} = \begin{pmatrix} -\Delta_h & 0 & 0 \\ 0 & -\Delta_h & 0 \\ (\partial_x)_{h/2} & (\partial_y)_{h/2} & -\Delta_h \end{pmatrix}.$$

Note that for the particular parameter selection (which is of no physical relevance) $\lambda = -1$, $\mu = 1$, and $\tilde{a} = 0$, (5) and (17) coincide with $\mathbf{L}_{h,st}$ and $\mathbf{C}_{h,st}$, respectively. Regarding this matter, the distributor for the poroelasticity model operator can be considered as a generalization of the well-known distributive relaxation for the staggered version of the Stokes equations.

3.4. Optimal Multigrid Smoothing for the System of Poroelasticity

The smoothing method S_h in a multigrid algorithm is designed to reduce high-frequency components of the error between exact solution and current approximation effectively. A quantitative measure for its efficiency represents the smoothing factor obtained by Fourier analysis. Fourier smoothing analysis is based on the observation that many classical relaxation methods (like Jacobi or Gauss-Seidel relaxation) leave the spaces of $2h$ -harmonics invariant, i.e.,

$$S_h|_{F_{2h}(\theta)} =: \tilde{S}_h(\theta) \in \mathbb{C}^{12 \times 12} \quad (\theta \in \Theta_{\text{low}}^{2h}).$$

Applying an “ideal” coarse grid correction operator

$$Q_{h,2h}|_{F_{2h}(\theta)} =: \tilde{Q}_{h,2h} = \text{diag}\{0, 0, 0, 1, 1, 1, 1, 1, 1, 1, 1, 1\} \in \mathbb{C}^{12 \times 12}$$

which annihilates the low-frequency error components and leaves the high-frequency components unchanged yields the smoothing factor [2], [14]

$$\rho_1(\mathbf{L}_h, n) := \sup_{\theta \in \Theta_{\text{low}}^{2h}} \rho\left(\tilde{Q}_{h,2h} \tilde{S}_h^n(\theta)\right),$$

i.e., the asymptotic error reduction of the high-frequency error components by n sweeps of the relaxation method. Here, $\rho(M)$ denotes the spectral radius of the matrix M . In analogy to the two-grid factor to be defined below, it could also be named *one-grid factor* as it only takes the fine grid operators-relaxation and discretization-into account. The subscript “1” refers to *one-grid*. For scalar equations, we have $\tilde{S}_h(\theta)$, $\tilde{Q}_{h,2h} = \text{diag}\{0, 1, 1, 1\} \in \mathbb{C}^{4 \times 4}$.

The smoothing factor $\rho_1(\mathbf{L}_h, n)$ for n distributive relaxations governed by (17) is determined by the diagonal blocks of the transformed system (18) [2], [14]. More precisely, we have

$$\rho_1(\mathbf{L}_h, n) = \max\left\{\rho_1\left(LC_h^{1,1} := -\mu\Delta_h, n\right), \rho_1\left(LC_h^{3,3} := \tilde{a}(\lambda + 2\mu)\Delta_h^2 - \Delta_h, n\right)\right\}. \quad (22)$$

This means that the calculation of $\rho_1(\mathbf{L}_h, n)$ reduces to the computation of the spectral radii of certain (4×4) -matrices. Both scalar operators $LC_h^{1,1}$, $LC_h^{3,3}$ occurring in (22) are *isotropic* in the sense that the coefficients referring to different spatial directions are of the same size. Hence, a distributive *point* relaxation method can be used for all choices of λ , μ , and \tilde{a} as it was already anticipated by the measure of h -ellipticity.

There are many efficient relaxation schemes known for $LC_h^{1,1}$. The smoothing properties of some of these schemes are, however, not satisfactory for $LC_h^{3,3}$, if it is dominated by the biharmonic term which depends on the set of parameters and the mesh size under consideration. More precisely, the corresponding smoothing factor increases for an increasing $\tilde{a}(\lambda + 2\mu)/h^2$. This can be observed for a fixed set of parameters λ , μ , \tilde{a} and a decreasing mesh size h . In Table 1 the smoothing factors are presented for red-black Jacobi (RB-JAC) point relaxation. Here, the computational grid is subdivided into red and black points in a checkerboard manner. RB-JAC consists of a Jacobi sweep over the red points only followed by a Jacobi sweep over the black points using the updated values at the red points.

Remark 4. Note, that RB-JAC coincides with the well-known Gauss-Seidel relaxation with a red-black numbering of grid points for 5-point discretizations like Δ_h . However, this equivalence is not longer valid for discrete operators based on “larger” stencils like Δ_h^2 ; see Remark 5.4.5 from [14] for details.

RB-JAC is the basis for very efficient multigrid methods for the Poisson equation [13], [14] which is demonstrated by the smoothing factor 0.25. However, for the biharmonic operator a deterioration to $\rho_1(\Delta_h^2, 1) = 0.64$ can be observed. For $LC_h^{3,3}$, the parameters λ , μ , and \tilde{a} are fixed and the mesh size h varies between $1/4$ and $1/256$. The choices for these parameters are representative for geophysical applications. Table 1 shows that the smoothing properties for $LC_h^{3,3}$ deteriorate with a decreasing mesh size (i.e., with increasing $\tilde{a}(\lambda + 2\mu)/h^2$) as the biharmonic term dominates.

Table 1. Smoothing factors $\rho_1(\cdot, 1)$ for three operators; $\lambda = 1250$, $\mu = 12500$, $\tilde{a} = 10^{-7}$

h	$\frac{1}{4}$	$\frac{1}{8}$	$\frac{1}{16}$	$\frac{1}{32}$	$\frac{1}{64}$	$\frac{1}{128}$	$\frac{1}{256}$
$-\Delta_h$	0.25	0.25	0.25	0.25	0.25	0.25	0.25
Δ_h^2	0.64	0.64	0.64	0.64	0.64	0.64	0.64
$\tilde{a}(\lambda + 2\mu)\Delta_h^2 - \Delta_h$	0.31	0.41	0.54	0.61	0.63	0.64	0.64

Improved smoothing factors can be obtained by introducing a *one-stage* parameter ω in RB-JAC. A one-stage variant of an arbitrary relaxation method S_h is given by

$$S_h(\omega) := (1 - \omega)I_h + \omega S_h$$

with discrete identity I_h . To construct an optimal one-stage relaxation, we search for the parameter ω which minimizes the corresponding smoothing factor. This means that one has to solve the following minimization problem:

$$\min_{\omega} \sup_{\theta \in \Theta_{\text{low}}^{2h}} \rho\left(\tilde{Q}_{h,2h}\tilde{S}_h(\omega, \theta)\right) \quad (23)$$

with $\tilde{S}_h(\omega, \theta) := (1 - \omega)\tilde{I}_h + \omega\tilde{S}_h(\theta)$ and identity matrix $\tilde{I}_h \in \mathbb{C}^{4 \times 4}$ (for the scalar case). The situation is particularly transparent, if we assume a non diverging relaxation S_h equipped with a real-valued “high-frequency spectrum”

$$\sigma_S := \left\{ \text{spectrum of } \tilde{Q}_{h,2h}\tilde{S}_h(\theta) \mid \theta \in \Theta_{\text{low}}^{2h} \right\},$$

i.e., $\sigma_S \subset [S_{\min}, S_{\max}] \subset [-1, 1]$. Then, (6) reduces to a classical minimization problem,

$$\min_{\omega} \sup_{-1 \leq S_{\min} \leq z \leq S_{\max} \leq 1} |(1 - \omega) + \omega z|;$$

see, for example, [15]. The optimal *smoothing* one-stage parameter and the related smoothing factor are given by

$$\omega_{\text{opt}} = \frac{2}{2 - S_{\max} - S_{\min}} \quad \text{and} \quad \rho_1(\cdot, n = 1) = \frac{S_{\max} - S_{\min}}{2 - S_{\max} - S_{\min}}. \quad (24)$$

Remark 5. Note, that the one-stage parameter is applied *after* a complete RB-JAC step (and not-as usual overrelaxation parameters-within each half step of RB-JAC relaxation). For Jacobi (JAC) relaxation, overrelaxation and one-stage parameter coincide since unknowns are updated *after* the complete relaxation sweep and not dynamically within the relaxation process (as for Gauss-Seidel or pattern relaxations like RB-JAC).

Example 1. As an example we consider Jacobi relaxation which is defined by

$$S_h^{\text{JAC}} := I_h - D_h^{-1}L_h,$$

where D_h denotes the diagonal part of some discrete operator L_h under consideration. Obviously, the Fourier components are eigenfunctions of S_h^{JAC} yielding a “diagonal” Fourier representation

$$\begin{aligned} \tilde{S}_h^{\text{JAC}}(\boldsymbol{\theta}) &= \text{diag}\{A_{00}, A_{11}, A_{10}, A_{01}\} \in \mathbb{C}^{4 \times 4} \quad \text{with} \\ A_x &= 1 - \tilde{D}_h^{-1}(\boldsymbol{\theta}^x) \tilde{L}_h(\boldsymbol{\theta}^x) \end{aligned} \quad (25)$$

for scalar operators L_h . For the Laplacian $L_h = -\Delta_h$ (11), we have $D_h \stackrel{\Delta}{=} \frac{1}{h^2} [4]_h$ leading to

$$A_x = 1 - \frac{h^2}{4} \tilde{\Delta}_h(\boldsymbol{\theta}^x) = 1 + \sin^2(\theta_1^x/2) + \sin^2(\theta_2^x/2) = \frac{1}{2}(\cos(\theta_1^x) + \cos(\theta_2^x)),$$

compare with (12). From the above Fourier representation of S_h^{JAC} , we easily obtain

$$\sigma_S = [S_{\min} = \frac{1}{2}(\cos(\pi) + \cos(\pi)) = -1, S_{\max} = \frac{1}{2}(\cos(-\pi/2) + \cos(0)) = 1/2].$$

Applying (24) yields the well-known optimal damped Jacobi smoother for the Laplacian:

$$\omega_{\text{opt}} = 4/5 \quad \text{and} \quad \rho_1(\Delta_h, n = 1) = 3/5.$$

For RB-JAC relaxation, the situation is somewhat more difficult as the Fourier components are no longer eigenfunctions of the relaxation operator. It still leaves the spaces of $2h$ -harmonics invariant, but certain Fourier components are coupled by RB-JAC yielding off-diagonal entries in its Fourier representation:

$$\tilde{S}_h^{\text{RB}}(\boldsymbol{\theta}) = \tilde{S}_h^{\text{B}}(\boldsymbol{\theta}) \cdot \tilde{S}_h^{\text{R}}(\boldsymbol{\theta}) \quad \text{with} \quad (26)$$

$$\tilde{S}_h^{\text{R}}(\boldsymbol{\theta}) = \frac{1}{2} \begin{pmatrix} A_{00} + 1 & A_{11} - 1 & 0 & 0 \\ A_{00} - 1 & A_{11} + 1 & 0 & 0 \\ 0 & 0 & A_{10} + 1 & A_{01} - 1 \\ 0 & 0 & A_{10} - 1 & A_{01} + 1 \end{pmatrix}, \quad (27)$$

$$\tilde{S}_h^{\text{B}}(\boldsymbol{\theta}) = \frac{1}{2} \begin{pmatrix} A_{00} + 1 & -A_{11} + 1 & 0 & 0 \\ -A_{00} + 1 & A_{11} + 1 & 0 & 0 \\ 0 & 0 & A_{10} + 1 & -A_{01} + 1 \\ 0 & 0 & -A_{10} + 1 & A_{01} + 1 \end{pmatrix}. \quad (28)$$

For the derivation of these Fourier representations for the consecutive Jacobi sweeps over the red (R) and the black (B) points, respectively, we refer to [13], [14].

Example 2. The optimal one-stage parameter for RB-JAC relaxation applied to Δ_h is given by $\omega_{\text{opt}}(\Delta_h) = 16/15$ leading to $\rho_1(\Delta_h, 1) = 1/5$, whereas for Δ_h^2 we

have $\omega_{\text{opt}}(\Delta_h^2) = 25/18$ yielding $\rho_1(\Delta_h^2, 1) = 1/2$; compare with Example 4.3.1 and Proposition 6.6.1 from [17], respectively. These results have been derived using $\tilde{S}_h^{\text{RB}}(\boldsymbol{\theta})$ with A_x from Example 1 for the Laplacian and with $A_x = 1 - \frac{h^4}{20}\tilde{\Delta}_h^2(\boldsymbol{\theta}^x)$ (see (11), (13)) for the biharmonic operator.

Since $LC_h^{3,3}$ is a combination of the two operators from Example 2, it is reasonable to search for an optimal one-stage RB-JAC relaxation for

$$LC_h^{3,3} = c\Delta_h^2 - \Delta_h \quad \text{with} \quad c = \tilde{a}(\lambda + 2\mu) \geq 0 \quad (29)$$

leading to the following theorem.

Theorem 2. *The spectrum σ_S (w.r.t. the high-frequency error components) of point RB-JAC relaxation applied to $LC_h^{3,3}$ (29) is bounded by*

$$S_{\min} = -\frac{16c^2 + 10ch^2 + h^4}{8(5c + h^2)^2} \quad \text{and} \quad S_{\max} = \frac{(8c + h^2)^2}{4(5c + h^2)^2}.$$

Proof: The Fourier representation $\tilde{S}_h^{\text{RB}}(\boldsymbol{\theta}) \in \mathbb{C}^{4 \times 4}$ for point RB-JAC relaxation applied to a two-dimensional operator like $LC_h^{3,3}$ is given in (26). After a projection onto the high frequency components using the ideal coarse grid correction operator $\tilde{Q}_{h,2h} = \text{diag}\{0, 1, 1, 1\}$ one obtains

$$\tilde{Q}_{h,2h}\tilde{S}_h^{\text{RB}}(\boldsymbol{\theta}) = \begin{pmatrix} 0 & 0 & 0 & 0 \\ a(\boldsymbol{\theta}) & b(\boldsymbol{\theta}) & 0 & 0 \\ 0 & 0 & d(\boldsymbol{\theta}) & e(\boldsymbol{\theta}) \\ 0 & 0 & f(\boldsymbol{\theta}) & g(\boldsymbol{\theta}) \end{pmatrix} \quad \text{with} \quad \boldsymbol{\theta} \in \Theta_{\text{low}}^{2h},$$

$$a(\boldsymbol{\theta}) = \frac{1}{4}(-A_{00}^2 + 1 + (A_{11} + 1)(A_{00} - 1)),$$

$$b(\boldsymbol{\theta}) = \frac{1}{4}(-(A_{00} - 1)(A_{11} - 1) + (A_{11} + 1)^2),$$

$$d(\boldsymbol{\theta}) = \frac{1}{4}((A_{10} + 1)^2 - (A_{01} - 1)(A_{10} - 1)),$$

$$e(\boldsymbol{\theta}) = \frac{1}{4}((A_{10} + 1)(A_{01} - 1) - A_{01}^2 + 1),$$

$$f(\boldsymbol{\theta}) = \frac{1}{4}(-A_{10}^2 + 1 + (A_{01} + 1)(A_{10} - 1)),$$

$$g(\boldsymbol{\theta}) = \frac{1}{4}(-(A_{10} - 1)(A_{01} - 1) + (A_{01} + 1)^2)$$

$$\text{and} \quad A_x = A(\boldsymbol{\theta}^x) = 1 - \frac{h^4}{20c + 4h^2} \left(c\tilde{\Delta}_h^2(\boldsymbol{\theta}^x) - \tilde{\Delta}_h(\boldsymbol{\theta}^x) \right); \quad (30)$$

compare with (27), (28), (25), (11), (12), and (13). The eigenvalues of $\tilde{Q}_{h,2h}\tilde{S}_h^{\text{RB}}(\boldsymbol{\theta})$ read $\lambda_1(\boldsymbol{\theta}) = 0$, $\lambda_2(\boldsymbol{\theta}) = b(\boldsymbol{\theta})$, and

$$\lambda_{3/4} = \frac{d(\boldsymbol{\theta}) + g(\boldsymbol{\theta})}{2} \pm \frac{1}{2} \sqrt{d(\boldsymbol{\theta})^2 + 4e(\boldsymbol{\theta})f(\boldsymbol{\theta}) - 2d(\boldsymbol{\theta})f(\boldsymbol{\theta}) + g(\boldsymbol{\theta})^2}.$$

A straight-forward but lengthy analysis yields that the spectrum σ_S of $\tilde{Q}_{h,2h}\tilde{S}_h^{\text{RB}}(\boldsymbol{\theta})$ ($\boldsymbol{\theta} \in \Theta_{\text{low}}^{2h}$) is real-valued. One may verify that the extreme values lie at the boundary of Θ_{low}^{2h} leading to

$$S_{\min} = \lambda_2(0, \pm\pi/2) = \lambda_2(\pm\pi/2, 0) = -\frac{16c^2 + 10ch^2 + h^4}{8(5c + h^2)^2}$$

and $S_{\max} = \lambda_3(0, \pm\pi/2) = \lambda_3(\pm\pi/2, 0) = \frac{(8c + h^2)^2}{4(5c + h^2)^2}.$

□

Corollary. *Using the above proposition and (24) we can construct an optimal one-stage method with one-stage parameter*

$$\omega_{\text{opt}}\left(LC_h^{3,3}\right) = \frac{16(5c + h^2)^2}{3(96c^2 + 46ch^2 + 5h^4)} \quad (31)$$

and optimal smoothing factor

$$\rho_1\left(LC_h^{3,3}, 1\right) = \frac{8c + h^2}{16c + 5h^2}. \quad (32)$$

Since $c = \tilde{\alpha}(\lambda + 2\mu) \geq 0$ and $h > 0$ it can be easily seen from (32) that

$$1/5 \leq \rho_1\left(LC_h^{3,3}, 1\right) \leq 1/2 \quad (33)$$

for all possible choices of $c = \tilde{\alpha}(\lambda + 2\mu)$ and h . More precisely, the lower bound is obtained if $c = 0$. Then $LC_h^{3,3}$ reduces to the Laplacian and the corresponding optimal one-stage method is given by $\omega(LC_h^{3,3}) = 16/15$ and $\rho_1(LC_h^{3,3}, 1) = 1/5$; see above. The upper bound is reached if the biharmonic operator dominates $LC_h^{3,3}$, i.e., $c/h^2 \rightarrow \infty$. For a fixed mesh size h this gives:

$$\lim_{c \rightarrow \infty} \omega_{\text{opt}}\left(LC_h^{3,3}\right) = \lim_{c \rightarrow \infty} \frac{16(25 + 10h^2/c + h^4/c^2)}{3(96 + 46h^2/c + 5h^4/c^2)} = \frac{400}{288} = \frac{25}{18},$$

$$\lim_{c \rightarrow \infty} \rho_1\left(LC_h^{3,3}, 1\right) = \lim_{c \rightarrow \infty} \frac{8 + h^2/c}{16 + 5h^2/c} = \frac{1}{2},$$

recovering the optimal one-stage method for the biharmonic operator.

The smoothing strategy is that the first two equations in (18) are smoothed by one-stage RB-JAC relaxation with $\omega_{\text{opt}}(\Delta_h)$, whereas for the third equation

$\omega_{\text{opt}}(LC_h^{3,3})$ is chosen, leading to the following smoothing factor for the system of poroelasticity:

$$\rho_1(\mathbf{L}_h, 1) = \max\left\{\rho_1(\Delta_h, 1), \rho_1\left(LC_h^{3,3}, 1\right)\right\} = \rho_1\left(LC_h^{3,3}, 1\right).$$

From (33) it immediately follows that

$$1/5 \leq \rho_1(\mathbf{L}_h, 1) \leq 1/2$$

which is a *strong robustness result* for such a complicated system involving several parameters $(\tilde{a}, \lambda, \mu, h)$. For example, two steps of the proposed RB-JAC one-stage method applied to the realistic set of parameters from Table 1 yields a satisfactory $\rho_1(\mathbf{L}_h, 2) = 0.25$.

Remark 6. The efficiency of many solution methods for problems from linear elasticity depends on the Poisson ratio ν defined in (3). The smoothing factor $\rho_1(\mathbf{L}_h, 1)$ only depends on the ratio c/h^2 and there is no particular difficulty caused by certain values for the Poisson ratio which is demonstrated by Tables 2 and 3. We use a fixed set of parameters for h, λ and \tilde{a} and vary μ in order to analyze the effect of the Poisson ratio. It can be clearly seen, that the smoothing factor is determined by c (for fixed mesh size) and is not affected by the often crucial value $\nu = 0.5$ for the Poisson ratio. For small values for c (due to $\tilde{a} = 5^{-7}$ in Table 2) the best possible smoothing factors are obtained independent of the Poisson ratio, whereas for large values for c (due to $\tilde{a} = 5^{-2}$ in Table 3) the worst possible smoothing factors are reached, again independent of the Poisson ratio. Summarizing, the robust behavior of the proposed relaxation method is independent of the Poisson ratio. Note that $\omega_{\text{opt}}(LC_h^{3,3})$ and $\rho_1(\mathbf{L}_h, 1)$ shown in Tables 2 and 3 result from a simple evaluation of (31) and (32), respectively.

Table 2. Poisson ratio ν and corresponding smoothing factor $\rho_1(L_h, 1)$ (up to three digits) for varying μ and fixed $\lambda = 1, \tilde{a} = 5^{-7}, h = 1/64$

μ	ν	c	$\omega_{\text{opt}}(LC_h^{3,3})$	$\rho_1(L_h, 1)$
1	0.25	$1.5 \cdot 10^{-6}$	1.072	0.206
10^{-1}	0.455	$6.0 \cdot 10^{-7}$	1.069	0.202
10^{-2}	0.495	$5.1 \cdot 10^{-7}$	1.068	0.202
10^{-4}	0.499	$5.001 \cdot 10^{-7}$	1.068	0.202

Table 3. Poisson ratio ν and corresponding smoothing factor $\rho_1(L_h, 1)$ (up to three digits) for varying μ and fixed $\lambda = 1, \tilde{a} = 5^{-2}, h = 1/64$

μ	ν	c	$\omega_{\text{opt}}(LC_h^{3,3})$	$\rho_1(L_h, 1)$
1	0.25	0.15	1.389	0.499
10^{-1}	0.455	0.06	1.388	0.499
10^{-2}	0.495	0.051	1.388	0.499
10^{-4}	0.499	0.050	1.388	0.499

Remark 7. Applying S_{\min} and S_{\max} from Theorem 2 it is possible to construct *multi-stage* variants of RB-JAC relaxation (see, for example, [17]) with even better properties. However, it turned out in the Fourier two-grid analysis and in the numerical tests that it does not pay off to invest too much work into smoothing because the coarse grid correction cannot reduce the low-frequency error components equally well. Therefore, we focus on one-stage RB-JAC smoothing methods.

3.5. Coarse Grid Correction

An appropriate coarse grid correction on the Cartesian grid G_h consists of straightforward geometric transfer operators $R_{h,2h}$, $P_{2h,h}$, which are well-established in the field of computational fluid dynamics and direct coarse grid discretizations (i.e., coarse grid analogs of L_h). Since we use a staggered grid, we have to distinguish the transfer operators which act on the different grids G_h^j ($j = 1, 2, 3$), see Fig. 1. At u - and v -grid points we consider 6-point restrictions and at p -grid points a 9-point restriction. In stencil notation they are given by

$$R_{h,2h}^u \stackrel{\wedge}{=} \frac{1}{8} \begin{bmatrix} 1 & & 1 \\ 2 & \star & 2 \\ 1 & & 1 \end{bmatrix}_{2h}^{2h}, \quad R_{h,2h}^v \stackrel{\wedge}{=} \frac{1}{8} \begin{bmatrix} 1 & 2 & 1 \\ & \star & \\ 1 & 2 & 1 \end{bmatrix}_{2h}^{2h}, \quad R_{h,2h}^p \stackrel{\wedge}{=} \frac{1}{16} \begin{bmatrix} 1 & 2 & 1 \\ 2 & 4 & 2 \\ 1 & 2 & 1 \end{bmatrix}_{2h}^{2h},$$

respectively. The restriction operator for the defect in the p -equation differs from the usual one in solving the incompressible Navier-Stokes equations, because of the placement of pressure points at the vertices, whereas a cell-centered pressure grid is employed in fluid mechanics applications. As the prolongation operators $P_{2h,h}^{u/v/p}$, we apply the usual interpolation operators based on linear interpolation of neighboring coarse grid unknowns, dictated by the staggered grid (see, for example, sect. 8.7 in [14]). The pressure prolongation is the adjoint of its restriction.

3.6. Fourier Two-grid Analysis

The crucial observation in the classical Fourier two-grid analysis is that the two-grid operator (9) leaves the spaces of $2h$ -harmonics (10) invariant. Hence, the two-grid operator can be represented in Fourier space by a block matrix consisting of (4×4) -blocks for scalar equations and by (12×12) -blocks for our discrete system (5):

$$M_{h,2h}|_{F_{2h}(\boldsymbol{\theta})} =: \tilde{M}_{h,2h}(\boldsymbol{\theta}) = \tilde{S}_h^{n_2}(\boldsymbol{\theta}) \tilde{C}_{h,2h}(\boldsymbol{\theta}) \tilde{S}_h^{n_1}(\boldsymbol{\theta}) \quad (\in \mathbb{C}^{12 \times 12})$$

with Fourier representation $\tilde{C}_{h,2h}(\boldsymbol{\theta})$ of the coarse grid correction operator. For details on Fourier two-grid analysis and the derivation of $\tilde{C}_{h,2h}(\boldsymbol{\theta})$, we refer to [2,13,14] and especially to [3,11] for the analysis on staggered grids.

From the above representation, one may easily calculate the two-grid convergence factor as the supremum of the spectral radii from the related block matrices by a computer program:

$$\rho_2 := \sup_{\theta \in \Theta_{\text{low}}^{2h}} \rho(\tilde{M}_{h,2h}(\theta)).$$

4. Numerical Experiments

In this section, the robustness and efficiency of the distributive relaxation method is investigated by comparing the theoretically predicted convergence factors with the actually obtained numerical convergence. We choose a zero right-hand side, homogeneous boundary conditions and a random initial guess to avoid round-off errors. Local Fourier analysis, as discussed in the previous section, yields asymptotic convergence estimates since it is based on certain spectral radii. We measure the asymptotic numerical multigrid convergence during the first time step by performing 100 multigrid cycles and taking the average of the last 50 defect reduction factors:

$$\rho_k(\text{num}) := \sqrt[50]{\rho_k^{100} \cdot \rho_k^{99} \rho_k^{51}} = \sqrt[50]{\frac{res^{100}}{res^{51}}}$$

with $\rho_k^m = res^m / res^{m-1}$ and the maximum norm of the residual over the three equations in the system after the m th multigrid cycle:

$$res^m := \|r_{h,1}^m\|_\infty + \|r_{h,2}^m\|_\infty + \|r_{h,3}^m\|_\infty.$$

The subscript “ k ” denotes the number of grids involved in the multigrid solution method. V(1,1) denotes a V-cycle with one pre- and one post-relaxation, F(1,1) the corresponding F-cycle.

The insensitivity of the smoothing method to critical values for the Poisson ratio carries over to the complete multigrid solver. We fix parameter $a = 1$, yielding $\tilde{a} = 0.5\delta t$, due to the Crank-Nicolson time discretization. Tables 4 and 5 show theoretical predictions and numerically obtained convergence factors for the parameters $\lambda = 1, h = 1/64, 10^{-4} \leq \mu \leq 1$, and $\delta t = 10^{-6}$ (Table 4) and $\delta t = 10^{-1}$ (Table 5). Obviously, these factors are *independent* of the varying μ and thus independent of the varying Poisson ratio. Instead they are governed by c (for fixed mesh size): the smaller c , i.e., the smaller \tilde{a} , the better the convergence.

Results for more realistic sets of parameters are shown in Table 6. It can be clearly seen, that the two-grid analysis provides excellent estimates for the numerically observed F-cycle convergence involving six grids. Applying the computationally less expensive V-cycle leads to a slight increase of the multigrid convergence.

Table 4. Local Fourier analysis results and numerical convergence factors for varying μ and fixed $\lambda = 1$, $\delta t = 10^{-6}$, $h = 1/64$

μ	cycle	ρ_1	ρ_2	$\rho_6(\text{num})$
$1, 10^{-1}, 10^{-2}, 10^{-4}$	V(1,1)	0.04	0.11	0.16
$1, 10^{-1}, 10^{-2}, 10^{-4}$	F(1,1)	0.04	0.11	0.10

Table 5. Local Fourier analysis results and numerical convergence factors for varying μ and fixed $\lambda = 1$, $\delta t = 10^{-1}$, $h = 1/64$

μ	cycle	ρ_1	ρ_2	$\rho_6(\text{num})$
$1, 10^{-1}, 10^{-2}, 10^{-4}$	V(1,1)	0.25	0.25	0.31
$1, 10^{-1}, 10^{-2}, 10^{-4}$	F(1,1)	0.25	0.25	0.25

Table 6. Local Fourier analysis results and numerical convergence factors for various parameters and fixed mesh size $h = 1/64$

parameter set	cycle	ρ_1	ρ_2	$\rho_6(\text{num})$
$\lambda = 1250, \mu = 12500,$	V(1,1)	0.25	0.25	0.30
$\delta t = 10^{-6}$	F(1,1)	0.25	0.25	0.25
$\lambda = 0, \mu = 0.5,$	V(1,1)	0.25	0.25	0.28
$\delta t = 10^{-2}$	F(1,1)	0.25	0.25	0.24
$\lambda = 0, \mu = 0.5,$	V(1,1)	0.04	0.11	0.16
$\delta t = 10^{-6}$	F(1,1)	0.04	0.11	0.10
$\lambda = 1, \mu = 1,$	V(1,1)	0.25	0.25	0.31
$\delta t = 10^{-1}$	F(1,1)	0.25	0.25	0.25
$\lambda = 10^3, \mu = 10^4,$	V(1,1)	0.25	0.25	0.31
$\delta t = 10^{-1}$	F(1,1)	0.25	0.25	0.25

5. Conclusions

We provide a fast and accurate discrete solution for the incompressible variant of the poroelasticity equations, discretized on a staggered grid to deal with stability complications.

A robust distributive relaxation method for the system of poroelasticity equations has been introduced. The properties of the smoother were analyzed and optimized by Fourier smoothing analysis. With standard geometric transfer operators and direct coarse grid discretization, an efficient multigrid method, based on point-wise smoothing methods results.

The analysis of the multigrid method has been performed with classical multigrid Fourier analysis techniques. Their benefits have become clear in this work. The numerical multigrid results agree very well with the results from the Fourier analysis. This is an important gain by the analysis. The influence of different relaxation parameters on the multigrid convergence factor can be very well predicted. The main disadvantage of Fourier analysis may be that it is not straightforward to apply to non-Cartesian grid applications. However, the insights obtained for the Cartesian grid case are valuable for the development of efficient solvers for poroelasticity problems in more complicated domains.

References

- [1] Biot, M.A.: General theory of three dimensional consolidation. *J. Appl. Phys.* 12, 155–164 (1941).
- [2] Brandt, A.: *Multigrid techniques: 1984 guide with applications to fluid dynamics*. GMD-Studie Nr. 85, Sankt Augustin, Germany 1984.
- [3] Brandt A., Dinar, N.: Multigrid solutions to elliptic flow problems. In: *Numerical methods for partial differential equations* (Parter, S., ed.), pp. 53–147. New York: Academic Press, 1979.
- [4] Ehlers, W., Blum, J. (eds.): *Porous media: theory, experiments and numerical applications*. Berlin: Springer, 2002.
- [5] Gaspar, F.J., Lisbona, F.J., Vabishchevich, P.N.: A finite difference analysis of Biot's consolidation model. *Appl. Num. Math.* 44, 487–506 (2003).
- [6] Gaspar, F.J., Lisbona, F.J., Vabishchevich, P.N.: Stable finite difference discretizations for soil consolidation problems. (submitted).
- [7] Hackbusch, W.: *Multi-grid methods and applications*. Berlin: Springer, 1985.
- [8] Harlow F.H., Welch, J.E.: Numerical calculation of time-dependent viscous incompressible flow of fluid with a free surface. *Phys. Fluids* 8, 2182–2189 (1965).
- [9] Mow V.C., Lai, W.M.: Recent developments in synovial joint biomechanics. *SIAM Rev.* 22, 275–317 (1980).
- [10] Murad, M.A., Thomee, V., Loula, A.: Asymptotic behaviour of semidiscrete finite element approximations of Biot's consolidation problem. *SIAM J. Numer. Anal.* 33, 1065–1083 (1996).
- [11] Niestegge A., Witsch, K.: Analysis of a multigrid Stokes solver. *Appl. Math Comp.* 35, 291–303 (1990).
- [12] Santos, J.E., Douglas J. Jr., Calderon, A.P.: Finite element methods for a composite model in elastodynamics. *SIAM J. Numer. Anal.* 25, 513–532 (1988).
- [13] Stüben K., Trottenberg, U.: *Multigrid methods: Fundamental algorithms, model problem analysis and applications*. In: *Multigrid methods*. (eds.) Lecture Notes in Math. 960, pp. 1–176. (Hackbusch, W., Trottenberg, U. Berlin: Springer, 1982).
- [14] Trottenberg, U., Oosterlee, C.W., Schüller, A.: *Multigrid*. New York: Academic Press 2001.
- [15] Varga, R.S.: *Matrix iterative analysis*. Englewood Cliffs: Prentice-Hall 1962.
- [16] Wesseling, P.: *Principles of computational fluid dynamics*. Berlin: Springer 2001.
- [17] Wienands, R.: *Extended local Fourier analysis for multigrid: optimal smoothing, coarse grid correction, and preconditioning*. Ph.D. Thesis, University of Cologne, Germany 2001.
- [18] Wittum, G.: Multi-grid methods for Stokes and Navier-Stokes equations with transforming smoothers: algorithms and numerical results. *Num. Math.*, 54, 543–563 (1989).

Roman Wienands
University of Cologne,
Mathematical Institute
Weyertal 86-90
50931 Cologne, Germany
wienands@mi.uni-koeln.de

Francesco J. Gaspar
Departamento de Matemática Aplicada,
University of Zaragoza
Pedro Cerbuna 12
50009 Zaragoza, Spain
fjgaspar@unizar.es

Francesco J. Lisbona
Departamento de Matemática Aplicada,
University of Zaragoza
Pedro Cerbuna, 12
50009 Zaragoza, Spain
lisbona@unizar.es

Cornelis W. Oosterlee
Delft University of Technology,
Faculty of Information Technology Systems,
Department of Applied Mathematical Analysis
Mekelweg 4,
2628 CD Delft, the Netherlands
C.W.Oosterlee@math.tudelft.nl